JGR Solid Earth

RESEARCH ARTICLE
10.1029/2022JB025141

Moho and LAB Across the Western Alps (Europe) From P and S Receiver Function Analysis

S. Monna[1], C. Montuori[1], F. Frugoni[1], C. Piromallo[1], L. Vinnik[2], and AlpArray Working Group[3]

[1]Istituto Nazionale di Geofisica e Vulcanologia, Rome, Italy, [2]Institute of Physics of the Earth, Moscow, Russia, [3]The Authors of AlpArray Working Group Are Mentioned in Appendix A3

Key Points:

- Joint inversion of P and S receiver functions constrains the lithosphere-asthenosphere structure and Moho and Lithosphere-Asthenosphere Boundary (LAB) topography below the Western Alps
- Across the Ivrea Geophysical Body the colliding Eurasia and Adria lithospheres have a similar average thickness of 90–100 km
- Moho and LAB topographies are better reconciled with lithospheric detachment than with a continuous slab below the Western Alps

Supporting Information:

Supporting Information may be found in the online version of this article.

Correspondence to:

S. Monna,
stephen.monna@ingv.it

Citation:

Monna, S., Montuori, C., Frugoni, F., Piromallo, C., Vinnik, L., & AlpArray Working Group (2022). Moho and LAB across the Western Alps (Europe) from P and S receiver function analysis. *Journal of Geophysical Research: Solid Earth*, *127*, e2022JB025141. https://doi.org/10.1029/2022JB025141

Received 11 JUL 2022
Accepted 23 SEP 2022

Author Contributions:

Conceptualization: C. Piromallo, L. Vinnik
Formal analysis: S. Monna, C. Montuori, F. Frugoni
Investigation: C. Montuori
Methodology: S. Monna, L. Vinnik
Software: S. Monna, L. Vinnik
Supervision: L. Vinnik
Writing – original draft: S. Monna, C. Montuori, F. Frugoni, C. Piromallo

Abstract In spite of numerous active and passive seismological investigations, the existence of continuous or interrupted continental subduction below the Western Alps is still open to debate. Many of the observations focus on the Moho or the deeper part of the mantle, while reliable information on the Lithosphere-Asthenosphere Boundary (LAB) below the Alpine region is scarce. Exploiting the data from the dense, broadband AlpArray Seismic Network we present a set of Receiver Function (RF) measurements on the Moho and LAB of a region encompassing the Western Alps, which includes the Ivrea Geophysical Body (IGB), a fragment of mantle placed at a few kilometers depth at the collision margin between Eurasia and Adria plates. We derive seismic velocity profiles of the crust-uppermost mantle below each station down to about 250 km, through the joint inversion of P and S RF. We constrain the lateral variations of the Moho and LAB topographies across the colliding plates, and quantify the errors related to our measurements. Our results allow us to considerably expand the published data of the Moho depth and to add a unique set of new measurements of the LAB. Our observations show that Eurasia and Adria lithospheres have a comparable thickness (on average 90–100 km), and are colliding below the IGB, and that Eurasia is not presently continuously subducting below Adria. These observations suggest that there is a gap between the superficial (continental) European lithosphere and the deep (oceanic) lithosphere, confirming the discontinuous structure imaged by some seismic tomography models.

Plain Language Summary The Alps are one of the most studied orogenic systems but a number of questions remain unanswered, such as the existence of continuous or interrupted subduction of the Eurasian plate below the Adria plate in the Western Alps. To answer this question, it is necessary to assess the geometry (such as thickness and position) of the two lithospheric plates that are involved. We use the receiver function technique on seismometer data coming from the dense AlpArray Seismic Network to explore the interfaces that delimit the shallow Earth layers: the Moho and the Lithosphere-Asthenosphere Boundary. Thanks to these measurements we were able to define the plate geometries below the Western Alps. Our observations show that Eurasia and Adria lithospheres have comparable (on average 90–100 km), that the plates are colliding, and that Eurasia is not presently continuously subducting below Adria. This information helps us understand the current state and recent geodynamic evolution of the Alps.

1. Introduction

The Alps are one of the most studied orogenic systems and the first case in which subduction and break-off of continental lithosphere have been proposed (Blanckenburg & Davies, 1995). The Alpine orogen is the product of the convergence between African and Eurasian plates, active from late Cretaceous onward, causing the subduction of the Ligurian-Piedmont and Valais oceans and the subsequent continental collision between Apulia (promontory of Africa) and Eurasia starting about 35 Ma ago (Dercourt et al., 1986; Stampfli et al., 2001).

Despite the great amount of data provided by past and recent seismological investigations (for a complete list see Hetényi et al., 2018), several open questions about the nature and deep structure of the lithosphere-asthenosphere system of the Alps remain, such as those pertaining to the slab continuity at depth beneath the western Alps. As of yet, seismological, geophysical, and geochemical data have not led to a conclusive model. According to Nocquet et al. (2016), given the absence of active convergence, the surface uplift observed in the northwestern Alps must result from deep-seated processes. Slab break-off is one of the mechanisms that has been embraced to explain the connection between the observations at the earth's surface and the dynamics in the deeper interior (e.g.,

Writing – review & editing: S. Monna, C. Montuori, F. Frugoni, C. Piromallo, L. Vinnik

Davies and von Blanckenburg, 1995). Spatial variations in elevation between different sectors of the Alps have been explained as being compatible with slab break-off (e.g., Fox et al., 2015) but also with continuous subduction below the Western Alps (e.g., Liao et al., 2018; Malusà et al., 2021). Other data, such as magmatism and crustal shortening, are not able to confirm or exclude slab continuity or break-off (Kästle et al., 2020), and often the assumption that a preferred tomographic model is representative of the actual structure affects the choice between these two scenarios. Some of the recent seismic tomography works favor the presence of break-off or tears in the slab (Beller et al., 2017; Kästle et al., 2018; Lippitsch et al., 2003; Paffrath et al., 2021), while others propose instead continuous subducting lithosphere (Lyu et al., 2017; Zhao et al., 2016, 2020). The 50–200 km depth range, which is crucial for understanding tectonic processes and where break-off might be inferred, is not clearly constrained by seismic tomography. Teleseismic body-wave models suffer from vertical smearing and need adequate crustal corrections, while surface-wave models have relatively little horizontal sensitivity at these depths. For these reasons a detailed 3D geometry of slab segments, their gaps, and the relative velocity contrasts, still remains elusive.

The receiver function (RF) techniques, based on the mode conversion at an interface of P-to-S (PRF) and S-to-P (SRF) body waves, are methods that are particularly suited to determine the existence and depth of (near) horizontal seismic discontinuities. Their sensitivity is therefore complementary to tomographic imaging, which is sensitive to 3D seismic velocity but smooths sharp boundaries. Previous regional-scale studies have been based mostly on PRF and focused on the Moho discontinuity below the Alps (e.g., Lombardi et al., 2008; Spada et al., 2013). More recently, Zhao et al. (2015) applied the PRF technique to data from the dense CIFALPS profile across the western Alps, imaging a positive-polarity converted phase down to 75 km depth, attributed to the Moho interface, that they considered as evidence for a continuous slab. Geissler et al. (2010), applied for the first time the SRF technique to determine the Moho and the LAB below a wide area of central Europe, although no clear signal was identified from the LAB below the few stations considered in the Alps. The latest work, by Kind et al. (2021), based on automated analysis of broadband S-to-P converted signals from permanent and temporary stations of the AlpArray Seismic Network (Hetényi et al., 2018), reconstructed the Moho topography along the Alpine chain and highlighted a broad vertical layer with a velocity reduction (negative seismic velocity gradient) down to 140 km depth below the European lithosphere, expected to mark the lithosphere–asthenosphere boundary.

Our study, based on both P and S receiver function analyses, focuses on an area that comprises the Western Alps, includes the high-density, high-velocity Ivrea Geophysical Body (IGB), and the boundaries between the Eurasian and Adriatic tectonic plates (Figure 1). We derive the structure of the crust and uppermost mantle through the joint inversion of P and S receiver functions calculated on data from the dense AlpArray Seismic Network (Hetényi et al., 2018). The method applied in this work is an evolution of the method that Monna et al. (2019) applied to some stations of the peri-Tyrrhenian region; in particular, while the direct part of the procedure is the same, we have implemented a different, improved methodology in the inversion part based on the Tsallis statistics (Tsallis, 1988; Tsallis & Stariolo, 1996). Without assuming an a priori velocity model, we are able to obtain seismic velocity profiles below each station down to about 250 km, follow in three dimensions the variations of the Moho and LAB across the colliding plates, and give a quantitative estimate of the errors related to our measurements. Our work expands the published measurements of the Moho depth offering a coherent topography, and adds an unprecedented set of measurements of the LAB.

2. Data and Methods

2.1. Data Selection and Receiver Function Calculation

With the RF analysis, it is possible to detect seismic phases that are converted at the Earth's discontinuities. The information extracted from the RF analysis can help us understand the seismic properties of the Earth's layers where the phase conversion takes place. Depending on the phase converted at seismic discontinuity *d*, two types of RFs can be calculated, that is, P*d*s and S*d*p. The S receiver functions are more suited than P receiver functions for studying the mantle lithosphere since they are free of S-wave multiple reflections. More detailed information on Ps and Sp RF processing can be found in Vinnik (1977) and Farra and Vinnik (2000).

We calculate the receiver functions (RF) on waveforms recorded by a subset of stations of the Z3 broadband AlpArray Seismic Network (2015) (AASN) distributed in the western Alps, over an area enclosing the Ivrea

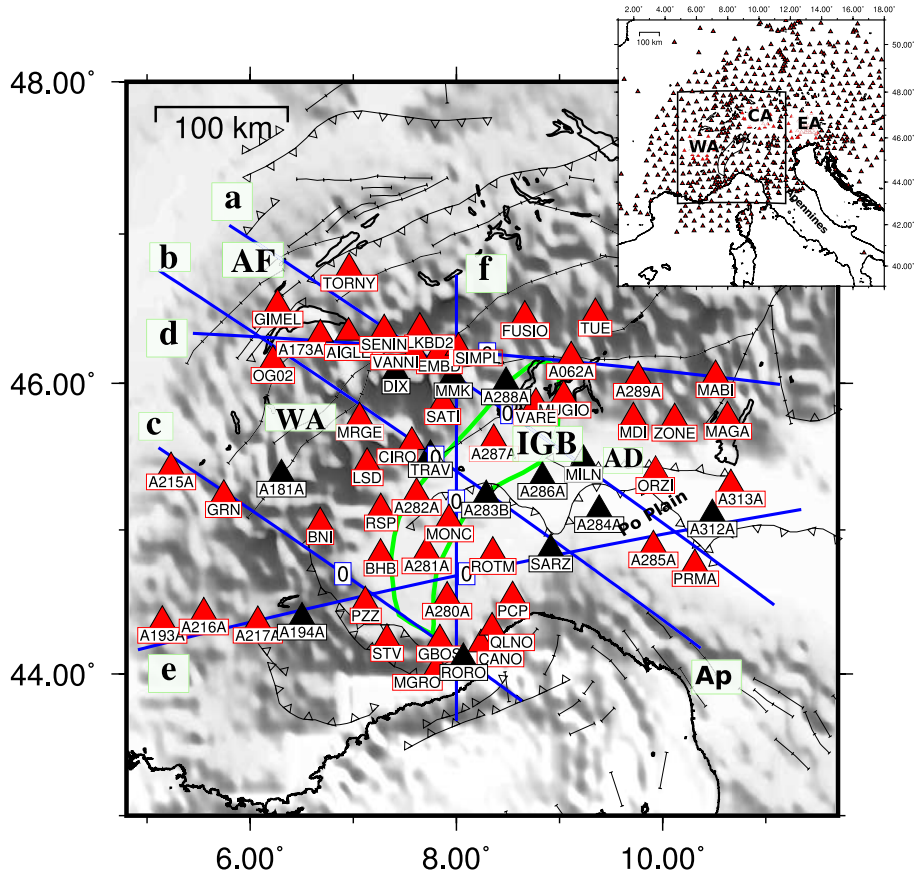

Figure 1. Inset: Triangles represent stations of the AA seismic network and the rectangle includes the study area. Main panel: Triangles indicate analyzed seismic stations (temporary and permanent). Black triangles are the analyzed and excluded stations. Blue lines represent the cross-sections' traces shown in Figure 4, the symbol zero marks the center of the trace. AF, Alpine front; WA, Western Alps; CA, Central Alps; EA, Eastern Alps; Ap, Apennines; IGB, Ivrea Geophysical Body; AD, Adria. The outline (green line) of the IGB is digitized from Wagner et al. (2012).

Geophysical Body. Figure 1 shows the temporary and permanent broadband stations used for this study. We selected teleseismic events ($M \geq 6$) in the time interval 2000–2021.

Since the Ps and Sp signals are usually very small, waveforms from several teleseismic events are stacked to enhance the converted phases (e.g., Kind & Vinnik, 1988). Our analysis is based on careful manual processing of thousands of P and S receiver functions and is an alternative to automated receiver function calculation. An accurate selection procedure, which often greatly reduces the initial data set, is applied to obtain reliable signals for the RF stacks. Since we have data from both permanent and temporary stations there is a wide range of recording periods available, from about 20 years (permanent) and from 1.5 up to 3 years (temporary) AASN stations. The first selection on the waveforms comes from the range of acceptable epicentral distances (30°–100° for the P and 65°–90° for the S) producing an initial number of about 50 P waveforms and 25 S waveforms in a year per station, on average. The analyst checks each raw waveform and discards the ones that are greatly affected by noise. The signal-to-noise ratio of the waveforms is improved by high-pass (30 s) and low-pass (6 or 8 s) filtering. The PRFs in some parts of the study area (e.g., Po Plain) are very noisy due to expected crustal reverberations. Noisy P and S RF are discarded after visual inspection, before stacking. The SRF are stacked by applying weights that depend on the level of noise, following Farra and Vinnik (2000) and Vinnik and Farra (2007)). Other details of the processing can be found in Monna et al. (2019). After this stringent selection, for some stations, it was not possible to obtain P or/and S receiver function stacks due to the lack of a sufficient number of acceptable traces. The number of RFs (P or S) is determined as sufficient when there is a clear well focused Moho signal and the stack is considered reliable and used for the inversion procedure. The black triangles in Figure 1 are excluded stations that do not have any reliable stack (P or S RF) according to our analysis. A stack is excluded when not even the Moho

signal is detectable in a reliable way. For some of the excluded stations, due to both random and signal-generated noise (such as crustal reverberations), it was not even possible to select a single receiver function.

2.2. Inversion Scheme

The high non-linearity and non-uniqueness of the RF inverse problem (Ammon et al., 1990) can benefit from non-linear global optimization algorithms that search large parameter spaces to identify global minima (Bodin et al., 2012). Global joint inversion of P and S RF for the upper 300 km has been successfully applied in various geodynamic contexts (e.g., Monna et al., 2019; Morais et al., 2015; Silveira et al., 2010; Vinnik et al., 2012). The Ps and Sp phases at the same epicentral distance sample the same Earth volume at different incidence angles, hence the PRF and SRF are complementary (Vinnik et al., 2004). In addition, since the Sp and Ps conversions depend on both Vp and Vs, the simultaneous inversion of P and S RF leads to a better-constrained model (Kiselev et al., 2008).

Velocity profiles below each station are calculated by simultaneous non-linear inversion of P and S receiver functions (RF). The forward part of the process was described in detail in a previous paper (Monna et al., 2019). In this work we improve the inversion scheme by:

1. Including a new more suitable (for our problem) version of the simulated annealing algorithm, the generalized simulated annealing (Tsallis, 1988; Tsallis & Stariolo, 1996). More information can be found in the Appendix A1.
2. Applying an optimal definition of the parameter space through sensitivity analysis (Section 2.3 and Appendix A2) and
3. Adding a parameter error estimate (Section 3.2).

Unfortunately, given the small number of selected RF, we cannot separate the data within different azimuthal sectors, although for a few stations it has been possible to calculate the PRF in two different azimuthal sectors. In our analysis we assume that the Earth below each station is laterally homogeneous and isotropic in the upper 300 km. For this reason we try to not over-interpret our models, which are a horizontal average within each layer, and focus on the depth of the Moho and LAB discontinuities. We should keep in mind that the phase conversion takes place in a finite area, which can be approximated as the intersection of the seismic discontinuity with the (first) Fresnel volume (e.g., Spetzler & Snieder, 2004). At a depth less than 300 km, the Fresnel zones for Ps and Sp of events from the same azimuthal sectors are for most stations either adjacent or overlapping; this is particularly true for the discontinuities we are investigating (<150 km). In cases where P and S RF are not sampling the same region, we should consider the model coming from the joint inversion as representative of the average seismic properties of the combined Fresnel volumes.

2.3. Model Dimension

An important question in data inversion (and modeling in general) is "what is the number of parameters that are best able to model the system of interest?" A useful methodology to answer this question is Sensitivity Analysis (SA) and its generalization, the Generalized Sensitivity Analysis (GSA). SA performs a local search while GSA performs a global search on all the parameter space. Here we only give a very intuitive introduction of GSA and the application we used, more detailed information can be found in Appendix A2. In rough terms, the objective of GSA is to evaluate how a certain group of input variables affect the output variable. GSA contains methods that we can use to identify the parameters that are necessary to describe our system and the ones that have little or no relevance in this description. Different theoretical representations can be used to perform GSA. In our case, the input parameters are the n variables used to model the Earth (Vp and Vs values in each layer and the layer thickness) and the output is the misfit, also called energy function, between the observed P and S receiver functions (stacks) and the theoretical receiver functions calculated from each model. The choice of the model should be driven by an "economy principle," in the sense that we should choose the minimum number of input parameters that allow us to adequately describe the system, which in the case of data inversion means to achieve a "good" fit to the observations. A way to formulate this problem is by determining which of the input parameters are more important in influencing the uncertainty in the model output, whose variance can be taken as a descriptor of output uncertainty (Saltelli et al., 2008). In the formulation given by Sobol, (1993, 2001), the variance of the output is decomposed ad hoc to quantify how the individual parameters influence the variance of

the output by themselves and through reciprocal interaction with the other parameters. From this decomposition we can calculate for each parameter sensitivity indices that measure its influence on the output. Thanks to this powerful approach we can answer the following questions that can help us choose the correct parameterization: is this parameter important in our problem? How important is it? Which parameters can we eliminate since their global sensitivity indices are below a threshold, showing that they have a negligible effect on the output (i.e., the misfit or energy function)? The application of GSA helped us decide that an Earth model with 5 layers described by 15 parameters is sufficient for our inversion procedure.

3. Results

3.1. Receiver Function Stacks and Seismic Station Classification

In this work, as a further improvement after Monna et al. (2019), we transparently attributed a quality factor to our stations. We classified stations according to the combined quality of the P and S receiver functions stacks. The PRF stacks were classified according to S/N ratio and the reliability of the Moho signal (Pms) detected on the stack (Table 1). The S/N is calculated in the following way for PRF: the noise is the average noise of the stacked Q traces (the direction that maximizes the SV component) before time zero (P mother wavelet arrival), while the signal is the Pms amplitude. A PRF is defined as class A if the S/N is >3 and the Moho signal is well detected and focused. For most stations the normalized amplitude of the signal Pms is 0.1–0.15. This signal is considered well focused if the greatest amplitudes occur at smaller depths in the stack, with the maximum at zero depth and identified with a red arrow as a bump of positive polarity between 2 and 7 s (Figure 2a).

Also the SRF stacks are classified according to noise and the quality of the Moho signal. The noise on the SRF signals is the RMS value calculated between −60 and −20 s (Farra & Vinnik, 2000). An SRF stack of class A has a well detected Moho signal (Smp), well-focused (maximum at 0°/s slowness) and with amplitude >3*noise (the noise level calculated to weigh the RFs for the stack). The stations are then classified according to the combined quality of P and S RF stacks (Table 1). A station of class A has both P and S RF of class A; a station of class B has either the P or the S RF stack of class A. Stations that do not have any reliable stack (P or S RF) are excluded. Excluded stations (black triangles in Figure 1) are mostly located, not surprisingly, in the western Alps and the Po plain, where Alpine thick sediments and strong crustal heterogeneity are present, confirming the experience of earlier studies based on the S receiver function technique (e.g., Geissler et al., 2010).

Figure 2 shows a selection of PRF and SRF stacks from stations that represent four tectonic domains: (1) Alpine front (2) Western Alps (3) IGB and (4) Adria. In the SRF stacks (Figure 2b), the Moho signal is clearly seen as a bump of negative polarity (between −2 and −7 s, identified by a black arrow). Other examples of P and S RF stacks are shown in Figure S1 in Supporting Information S1. For several stations it is also possible to identify a candidate signal converted at the LAB directly on the stack (positive polarity bump at about −10 s, identified with a green arrow). This signal is considered reliable if its amplitude is greater than 3* noise (see Data and methods), if the amplitude is greater than the Moho sidelobe found at positive times, and its time is called Tlab (Table 1). This signal was also identified in a similar way on SRFs calculated in Central and Eastern Europe by Geissler et al. (2010).

3.2. Velocity Models and Vertical Errors

We obtain velocity-depth profiles for 50 stations. In Figure 3 are the velocity-depth profiles for the eight example stations of Figure 2 that represent the tectonic domains identified in the study area (Figure 1). Once a best-fitting model (or set of models) is identified by the inversion procedure, it is desirable to associate an estimate of reliability to the model parameter value. In our case this estimate is especially important for the LAB depth, since it is derived from a small amplitude signal (compared to the Moho signal). The estimate is the result of several steps, each one affected by error. The final error affecting the estimate of our model parameters is the composition of a series of uncertainties that propagate along the whole process. Unfortunately, we cannot calculate this (absolute) error since an analytic error propagation derivation is not available. We try therefore to control and minimize the errors in the various steps and to associate an error to our final parameter estimate. First we discard unreliable raw waveforms by visual inspection as described earlier. We then calculate the receiver functions and their stack from which we extract the two waveforms that the inversion procedure will try to fit. The erroneous calculation of these waveforms will lead to a systematic error that, even if the inversion is successful (good fit), will lead

Table 1
Data for Analyzed and Accepted Stations (Class A and B)

Station	LAT	LON	t Ps Moho (s)	A *Ps* Moho	N traces	S/N	t *Sp* Moho (s)	A *Sp* Moho	N traces	Sigma	Tlab (s)	A *Sp* LAB	Depth Moho (km)	Vertical error (km)	Depth LAB (km)	Vertical error (km)	Quality
A062A	46.181	9.113	5.7	0.115	8	3.03	−4.2	−0.080	7	0.020	–	–	36.1	3.8	–	–	B
A173A	46.329	6.680	3.1	0.110	21	3.24	−3.6	−0.182	8	0.014	−8.5	0.080 ?	30.8	3.0	76.6	8.4	A
A181A	45.380	6.302	7.2	0.075	7	3.95	−3.75	−0.077	6	0.023	–	–	35.8	3.0	–	–	B
A193A	44.371	5.148	2.6	0.223	7	4.06	−4.0	−0.230	6	0.015	−10.2	0.130	32.4	3.0	85.1	7.5	B
A215A	45.431	5.232	2.8	0.15	39	4.04	−3.9	0.10	7	0.016	–	–	29.2	3	67.2	7.5	B
A216A	44.429	5.550	3.1	0.244	12	3.39	–	–	–	–	–	–	29.5	5.4	–	–	B
A217A	44.370	6.073	3.1	0.109	8	3.11	−3.2	−0.112	4	0.024	−7.9	0.090	40.0	3.0	72.1	7.5	B
A280A	44.539	7.909	5.4	0.211	6	4.59	−5.2	−0.078	–	–	–	–	35.9	7.8	79.4	9.0	B
A281A	44.853	7.701	2.3	0.203	5	2.64	−3.1	−0.110	3	0.029	–	–	29.7	3.0	91.5	7.5	B
A282A	45.255	7.613	2.1	0.14	4	2.55	−4.0	−0.140	6	0.037	−11.7	0.090	30.7	3.0	94.4	7.5	B
A285A	44.894	9.901	2.2	0.371	12	3.60	−5.0	−0.150	4	0.016	–	–	39.7	5.8	121.8	10.0	B
A287A	45.623	8.361	2.7	0.242	9	6.05	−3.4	−0.124	8	0.017	−9.6	0.055 ?	29.0	3.0	84.7	7.5	A
A289A	46.047	9.761	5.5	0.115	10	6.11	−4.7	−0.10	9	0.030	–	–	39.6	3.0	91.8	7.5	B
A313A	45.313	10.662	2.0	0.367	8	3.75	−5.3	−0.124	9	0.017	−11.3	0.093	31.8	3.0	90.4	7.5	A
AIGLE	46.342	6.953	3.5	0.111	25	3.47	−5.0	−0.07	11	0.019	−9.8	0.080 ?	42.2	4.0	89.1	8.0	A
BHB	44.835	7.263	7.1	0.150	7	5.64	−4.1	−0.21	8	0.018	–	–	44	3.0	110.6	7.5	A
BNI	45.052	6.678	6.3	0.064	7	3.56	−3.6	−0.071	38	0.007	–	–	51.2	4.2	87.4	9.4	A
CANO	44.208	8.237	3.9	0.209	4	3.17	−4.1	−0.082	5	0.018	–	–	24.9	3.0	80.0	7.5	B
CIRO	45.602	7.568	6.7	0.105	13	6.18	−5.2	−0.07	23	0.001	−12.4	0.030	53.1	4.6	106.3	7.5	B
EMBD	46.216	7.832	6.4	0.133	41	4.03	−6.7	−0.087	10	0.014	−12.2	0.072	42.4	3.0	92.3	7.5	B
FUSIO	46.455	8.663	5.5	0.072	12	3.79	−4.7	−0.085	26	0.072	−10.5	0.037	44.9	4.4	86.9	9.8	A
GBOS	44.242	7.840	4.1	0.068	12	3.24	−3.8	−0.072	15	0.013	–	–	25.6	3.4	90.5	7.8	A
GIMEL	46.534	6.265	3.3	0.146	19	3.74	−3.8	−0.143	67	0.063	−8.4	0.076	26.7	3.0	72.3	7.5	A
GRN	45.241	5.744	3.3	0.146	19	3.74	–	–	–	–	–	–	33.2	3.0	–	–	B
LKBD2	46.375	7.644	4.6	0.086	9	3.31	−5.0	−0.070	10	0.017	−9.6	0.034	37.5	3.0	83.2	7.5	A
LSD	45.460	7.134	5.5	0.090	12	3.91	−3.7	−0.01	11	0.013	–	–	48.6	3.0	88.3	7.5	B
MABI	46.055	10.514	5.2	0.141	15	4.27	−3.7	−0.137	10	0.024	−10.8	0.087	38.2	3.0	87.2	7.5	A
MAGA	45.775	10.629	4.3	0.176	41	5.18	−4.3	−0.167	14	0.015	−10.9	0.060	32.0	4.8	89.3	12.0	A
MDI	45.769	9.716	3.9	0.125	18	3.47	−4.8	−0.013	16	0.014	–	–	34.8	3.4	117.5 ?	9.8	A
MGRO	44.042	7.808	3.5	0.106	12	3.12	−4.5	−0.120	7	0.019	−10.0	0.060	44.3	5.4	83.1	8.8	A
MONC	45.074	7.927	5.9	0.140	10	5.19	−4.3	−0.090	12	0.017	–	–	34.5	6.0	106.1	13.0	B
MRGE	45.770	7.061	5.5	0.120	37	5.22	−6.1	−0.068	29	0.008	−12.1	0.033 ?	41.6	9.2	104.6	12.2	A
MUGIO	45.920	9.040	4.4	0.139	11	3.27	−4.3	−0.088	9	0.017	–	–	36.9	3.2	99.0	12.8	A
OG02	46.154	6.220	2.6	0.149	27	3.73	−4.2	−0.116	10	0.020	−9.1	0.055	37.4	3.0	81.8	8.8	A
ORZI	45.406	9.931	6.6	0.376	5	3.92	−4.7	−0.155	-4.7	0.028	–	–	36.8	3.0	–	–	B
PCP	44.541	8.545	6.2	0.122	9	4.07	−5.0	−0.098	15	0.013	−11.0	0.050 ?	40.7	3.0	114.2 ?	7.5	A
PRMA	44.764	10.313	7.0	0.277	7	5.43	−4.4	−0.160	7	0.027	–	–	43.1	3.0	108.0	7.5	A
PZZ	44.507	7.116	3.9	0.093	12	2.82	−4.2	−0.157	37	0.007	−10.8	0.073	49.8	4.8	113.5	7.5	A
QLNO	44.324	8.346	2.9	0.163	25	3.54	−3.8	−0.172	55	0.007	−9.6	–	25.1	3.0	83.8	7.5	A
ROTM	44.849	8.353	1.9	0.321	8	4.01	−4.7	−0.170	10	0.023	−11.0	0.080 ?	35.0	4.0	89.4	7.5	B
RSP	45.148	7.265	6.8	0.129	12	5.16	−4.5	−0.180	9	0.018	−10.1	0.090	51.0	5.6	84.0	7.5	B

Table 1
Continued

Station	LAT	LON	t Ps Moho (s)	A *Ps* Moho	N traces	S/N	t *Sp* Moho (s)	A *Sp* Moho	N traces	Sigma	Tlab (s)	A *Sp* LAB	Depth Moho (km)	Vertical error (km)	Depth LAB (km)	Vertical error (km)	Quality
SATI	45.875	7.868	6.6	0.224	45	6.59	−5.6	−0.06	10	0.013	–	–	44.2	5.0	87.3	8.2	A
SENIN	46.363	7.299	3.5	0.070	14	3.33	−4.6	−0.070	13	0.018	–	–	39.0	3.0	88.5	7.5	B
SIMPL	46.240	8.019	5.7	0.231	9	6.08	−6.9	−0.070	10	0.010	−11.6	0.1	41.8	3.0	88.4	7.5	B
STV	44.245	7.326	5.9	0.127	15	3.53	−4.8	−0.130	13	0.016	−12.5	0.050	31.0	6.2	104.3	9.0	B
TORNY	46.774	6.959	2.6	0.190	69	3.88	−3.1	−0.130	29	0.009	−8.4	0.070	30.1	3.0	67.7	7.5	A
TUE	46.472	9.347	4.3	0.082	10	3.28	−4.5	−0.065	57	0.005	–	–	45.9	3.0	87.1	7.5	A
VANNI	46.210	7.597	6.2	0.096	24	3.69	–	–	–	–	–	–	47.6	4.0	–	–	B
VARE	45.868	8.770	3 .0	0.07	9	3.04	−4.2	−0.156	15	0.019	−10.1	0.1	39.9	3.8	90.8	7.5	B
ZONE	45.764	10.117	3.8	0.118	20	3.5	−4.8	−0.170	11	0.034	–	–	36.7	6.0	116.0 ?	10.0	B

Note. tPs (APs) are the Arrival Times (Normalized Amplitude) for the Ps Phases Converted at the Moho. tSp (ASp) are the Arrival Times (Normalized Amplitude) for the Sp Phases Converted at the Moho. Tlab (ASp LAB) Arrival Time (Normalized Amplitude) for the Candidate Phase Sp Phase Converted at the LAB (when Available). The Question Mark is Added When the LAB Phase has Amplitude Greater Than Noise 3*sigma but Smaller Than the Sidelobe Found at Positive Times (See Also Figure 2). For the Calculation of the S/N (Signal-To-Noise) and Sigma, See Station Classification in the Data and Methods Section).

to an unreliable model parameter estimate. To control and minimize such systematic errors, a careful receiver function selection and station classification is performed. In the final step we have the inversion procedure, where the parameter space is explored extensively through $\sim 10^5$ iterations. We try to avoid overfitting in a null model space (the part of the model space unaffected by the data) by determining the necessary number of parameters with the GSA analysis. Once the inversion is completed, we can plot each individual parameter versus energy values (Figure S2 in Supporting Information S1) and see the pattern of its distribution (which might be multi-modal). The set of models around the maximum is identified as the family of best-fitting models. We can then fit the distribution for each parameter with a Gaussian (Venables & Ripley, 2002) and the parameter estimate is the maximum (mean) of the Gaussian fit to the parameter distribution. The final error that we associate to the parameter estimate is proportional to the variance of the Gaussian. From numerous synthetic tests, with a set of four layered Earth models with Moho and LAB discontinuities, we find that the maximum error is 2 km for the Moho and 5 km for the LAB depth (Figure S3 in Supporting Information S1). In fact, the depth of the asthenosphere bottom is also well recovered. We consider as a choice of good-sense 1.5 times these values to be the lower limit for the errors associated with the measurements of the Moho and LAB depth from the real data inversion (i.e., 3 km and 7.5 respectively). Finally, we define (again as a choice of good-sense) the error associated with the calculated Moho or LAB depth as the maximum between two times the variance calculated in the Gaussian fit of the parameters and the lower limits derived from the synthetic tests (Table 1).

3.3. Wave Lateral Sensitivity

Another aspect of interest is the lateral sensitivity of the wave at discontinuity *d* where conversion, P*d*s or S*d*p takes place. Given that we are using finite frequency waves, we also calculate the extent of the first Fresnel zones as an estimate of the horizontal sensitivity of the waves converted at the discontinuities. This estimate of the sensitivity volume of the converted waves, together with the location of the piercing points, allows us to identify the sampled region below each station that is contributing to our measurements. We estimated the first Fresnel zones of the converted waves at the discontinuity (Moho or LAB), according to its definition (Cerveny, 2001), by calculating the dominant wave period of the P and S RF in each station stack. We tried, when possible, to lower the low-pass filter corner period to 6 s, but for many stations it was necessary to go to 8 s to have an acceptable stack. In any case, our synthetic tests show (Figure S3 in Supporting Information S1) that this inversion scheme allows the accurate recovery of Moho and LAB depth for a plane-layered Earth when data is low-pass filtered at 8 s. The piercing points and traveltimes of the seismic phases were calculated with the TauP Toolkit (Crotwell et al., 1999) in the IASP91 model. The first Fresnel zone radius is on average about 35 km for the Moho and 60 km for the LAB.

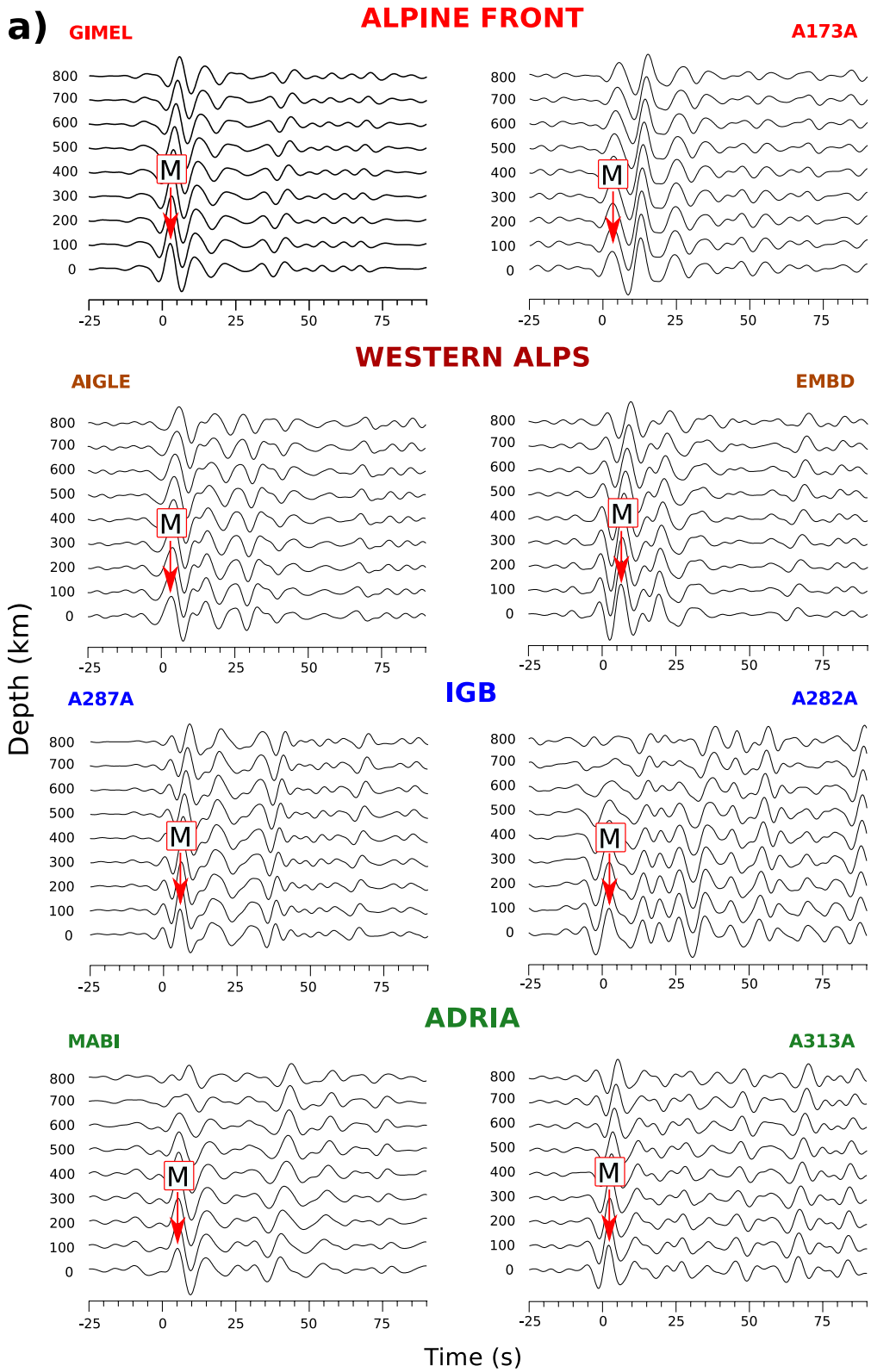

Figure 2.

Figure 4 shows a number of cross-sections (see profile traces in Figure 1) with estimated Moho and LAB depths for each station at the piercing points, together with the vertical error (vertical bar) and the first Fresnel zone (horizontal bar).

3.4. Moho and LAB Depth

Table 1 reports the estimates of the Moho and LAB depths below each station and its associated error in depth, on average 5 km for the Moho and 10 km for the LAB. The cross-sections in Figure 4 show the European Moho gently deepening from 30 to 35 km in the Alpine front to about 45–55 km below the Western Alps just west of the IGB. Below the IGB area we observe an abrupt shallowing of the Moho to 24–29 km. In the Adria sector the Moho depth ranges 32–42 km, with the deepest values below the Apennines. The blue line in the cross-sections represents an interpolation of the Moho depths published by Spada et al. (2013), based on PRF and controlled-source seismology (CSS) measurements.

The base of the European lithosphere, similarly to the Moho, deepens west to east, from ∼70 km in the foreland to 90–100 km below the western Alps (Figure 4). Below the IGB the detected LAB is at 80–90 km depth in the north (Figure 4a) and deeper in the southern part at ∼100 km (Figures 4b and 4c). The LAB depth of the Adriatic plate is in the depth range 85–100 km and deepest below the Apennines. For two stations in the Adria plate (MDI and ZONE) we find anomalously deep (with respect to the surrounding stations) LAB values, at about 115 km. Three nearby stations in the south of the IGB (CANO, QLNO and MGRO) show shallower LAB values compared to nearby stations.

The time Tlab of the inferred S-to-P conversion at the LAB observed at several stations (Table 1 and Figure 2b) spans from about 8 to 12.5s. The conversion to depth of these times depends on the seismic velocity structure below each station. The smaller Tlab times are found in the Alpine foreland where in fact shallow LAB depth values are found. Starting from the Alpine foreland, from W to E, the Tlab value grows attaining its maximum values just west of the IGB (Table 1).

4. Discussion

We calculated, by joint inversion of P and S receiver functions, the Moho and LAB depths below 50 stations of the AlpArray Seismic Network located in the Western Alps. Where a comparison was possible, the Moho depth values we estimated are generally in good agreement with previous studies based on published CSS and receiver function measurements (Figure 5a; Di Stefano et al., 2011; Lombardi et al., 2008; Spada et al., 2013; Wagner et al., 2012; Waldhauser et al., 1998), but we add information below the 14 temporary stations of the AASN that we analyzed. Recently, Kind et al. (2021) gave a provisional Moho depth estimate of about 65 km (along their profile 1) in the Western Alps, applying a new method to S-to-P conversions, the same seismic phase that we used in the calculation of the S-receiver function, but stacking instead raw untouched broadband data, without any filtering or deconvolution. Our Moho depth estimate in the Western Alps reaches a maximum of 53.7 ± 4.6 km (below station CIRO). Discrepancies, between Moho estimates by Kind et al. (2021) and our estimates could be ascribed to several factors, such as the different approach in data selection and processing, that is, automated versus manual, different methodology, that is, S-to-p converted waves migrated in depth vs global joint inversion of P-to-s and S-to-p receiver functions, and differences in the choice of the velocity model, considered as known a priori vs considered as unknown and determined through the inversion procedure.

As for the LAB, with our measurements we obtain a five-fold increase in the number of stations for which the LAB estimates are provided and a wider aerial coverage with respect to the SRF analysis by Miller and Piana Agostinetti (2012). Figure 5b points to a partial agreement between the values for the LAB depth estimated in this study and those obtained at sparse stations by Miller and Piana Agostinetti (2012). In the Western Alps, our estimates for the LAB, which is deepest at 106.3 ± 7.5 Km below station CIRO, agree within the error bounds, with the depth of the negative velocity gradient of Kind et al. (2021) dipping south to about 110 km (their Figure 3b).

Figure 2. P and S receiver function stacks from stations that represent the four tectonic domains: (1) Alpine front (2) Western Alps (3) IGB (4) Adria. (a) P-to-S (PRF) stacks; red arrows indicate the positive phase converted at the Moho interface (M). (b) S-to-P (SRF) stacks; black arrows indicate the negative phase converted at the Moho interface, the green arrow indicates the positive candidate phase converted at the Lithosphere-Asthenosphere Boundary (LAB); question marks are for phases that have amplitude greater than noise 3*sigma but smaller than the sidelobe found at positive times. The time moveout correction is calculated with respect to depth for the PRF and respect to slowness in the SRF.

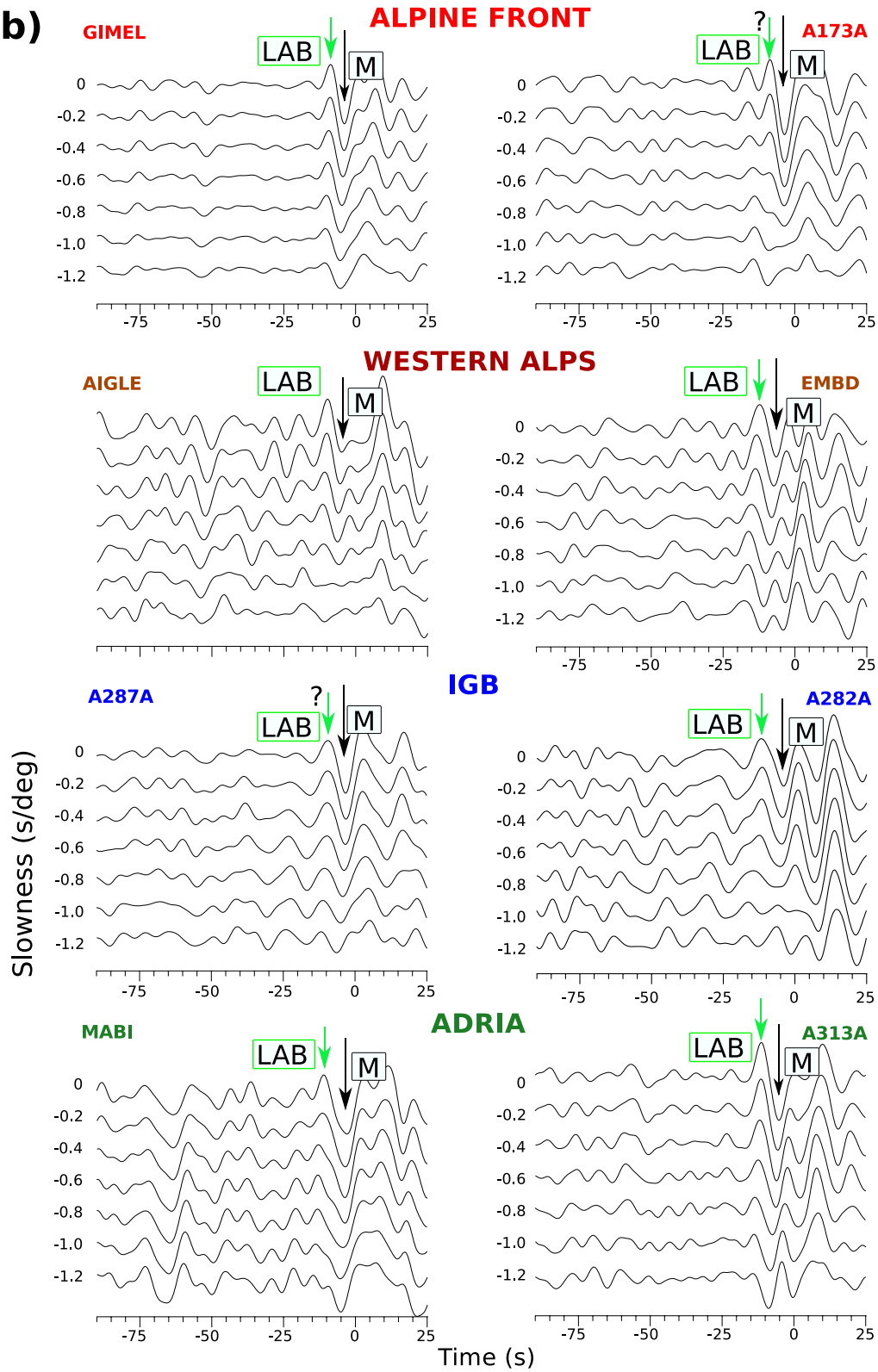

Figure 2. (Continued)

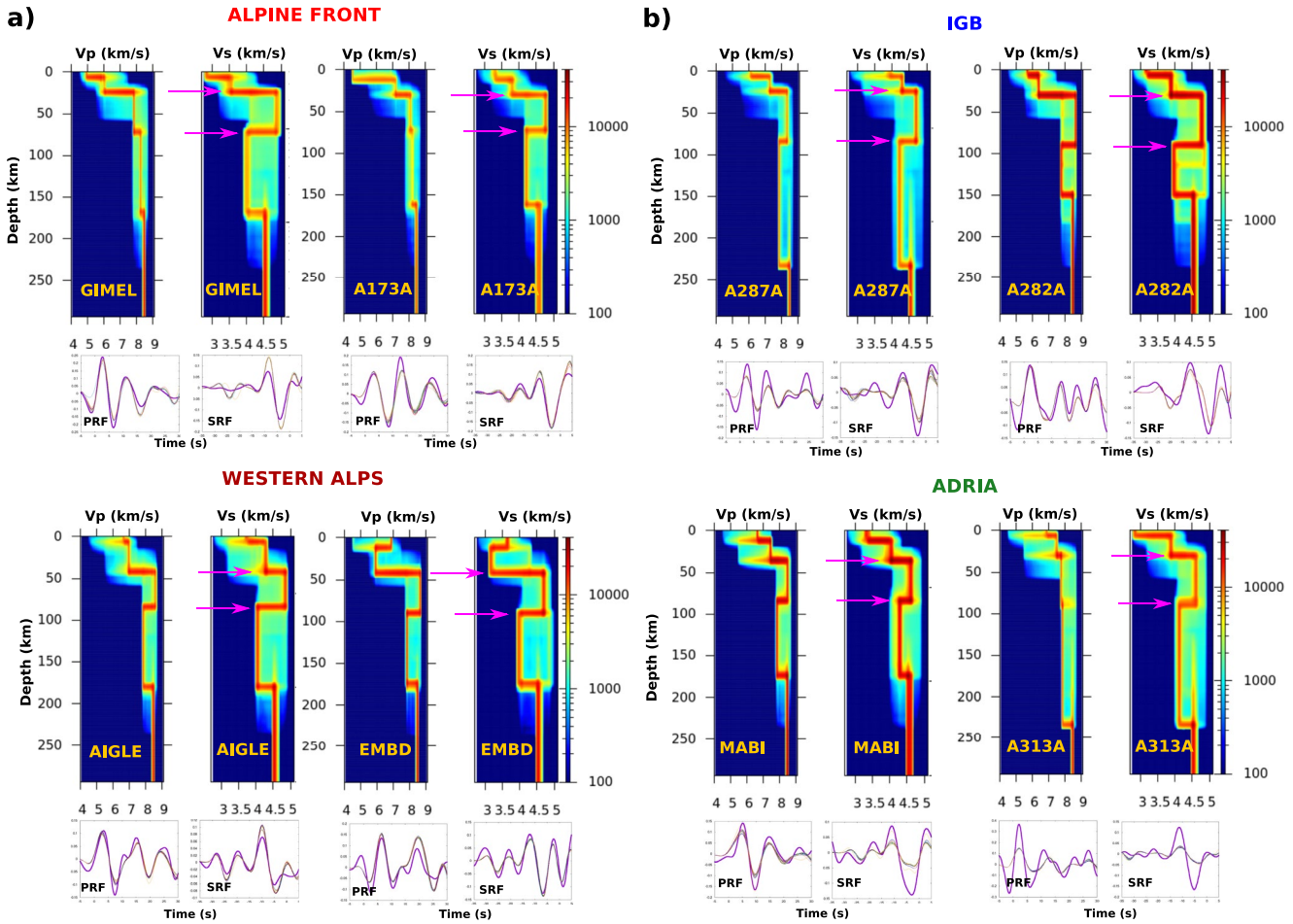

Figure 3. Heatplots for the Vs-versus depth models of the eight stations shown in Figure 2. The Moho and Lithosphere-Asthenosphere Boundary discontinuities are indicated by magenta arrows.Bottom panels, fit of the synthetic RFs calculated for the best 100 models, The observed RFs are the thick magenta curves.

Differences in the methodology and data selection procedure can explain why Kind et al. (2021) detect a low velocity zone below the LAB, while we detect a sharp lithosphere-asthenosphere discontinuity. One should keep in mind that the signals converted from the LAB are quite small (a few hundredths of the amplitude of the mother wavelet) and could get lost in the summation of a great number of waveforms with lower S/N within an automated procedure. Our analysis shows a gradual deepening of the European LAB (and Moho) going from west to east, up to the IGB (Figures 4 and 5). At the IGB the European Moho is deeper than the Adria Moho, and across the IGB the depths of the LAB of the two plates are similar, on the average 90–100 km. Figure 4e shows a profile that is close to the CIFALPS transect, and, although the European Moho does deepen below the Adriatic, down to roughly 50 km depth, we find that the two LABs have comparable depths, and do not exhibit significant dipping trends suggestive of subduction. Below the IGB we find a more superficial LAB signal associated with a depth of 80–85 km (Figure 4).

Beneath the Western Alps all tomography models image high seismic velocity heterogeneity below 120 km depth. Some authors interpret this heterogeneity as a detached lithosphere fragment at depth with no clear evidence of continuous subduction (Kästle et al., 2018; Lippitsch et al., 2003; Paffrath et al., 2021), while others interpret it as a continuous subducting slab (Lyu et al., 2017; Zhao et al., 2016, 2020). Some of the recent seismological evidence in support of continuous continental subduction below the Western Alps is in fact not very strong. In particular, Zhao et al. (2015) image a downgoing Moho interface from P receiver functions and interpret it as confirmation for a downgoing continuous slab, but the part of the profile that is proposed as evidence of the subducting slab down to about 75 km depth in the internal zone is composed of a weak signal with a very small amplitude, of the order of the noise amplitude. The weakness of this signal is very evident when looking at the

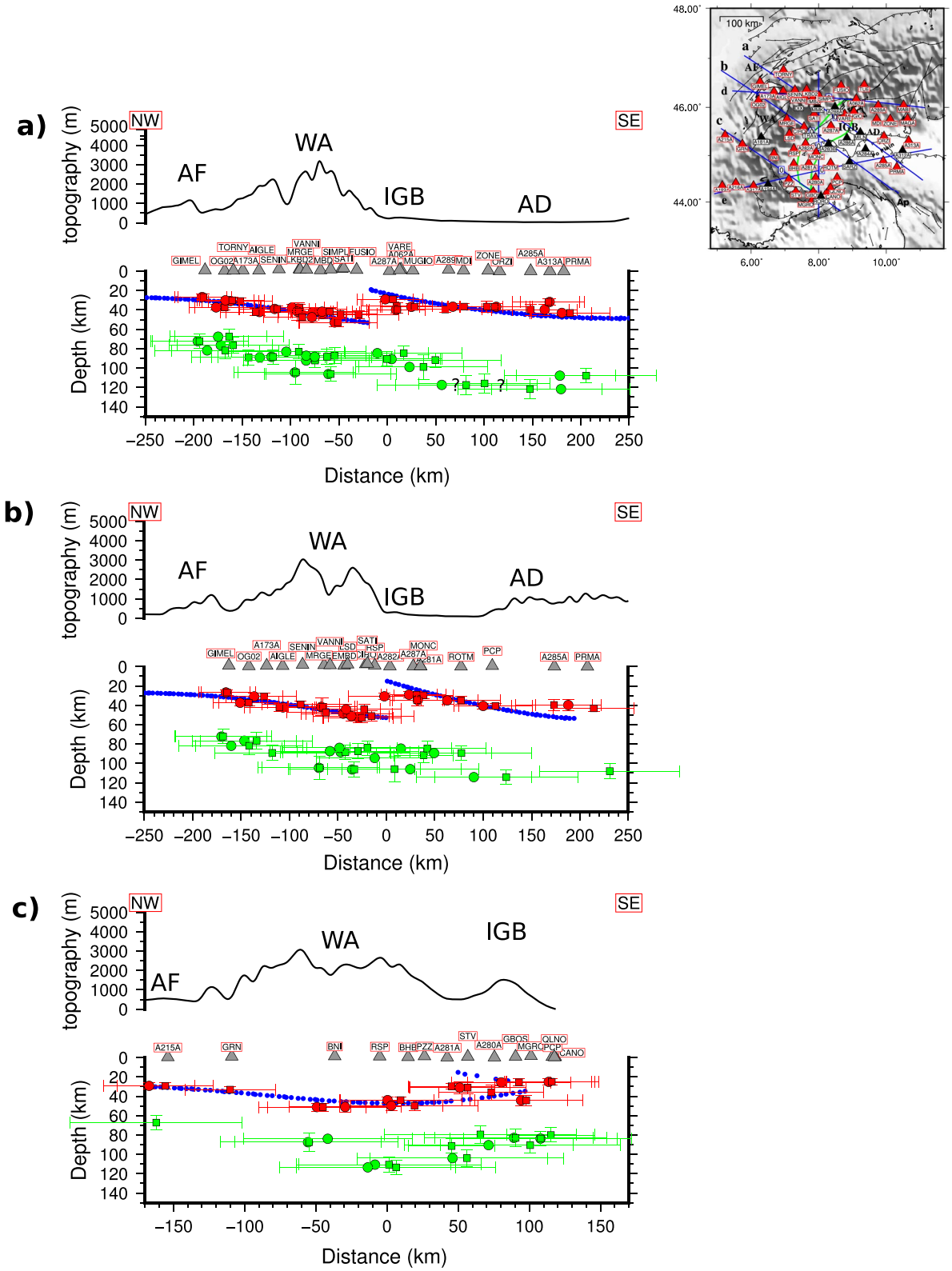

Figure 4.

receiver function raw stacks (used for the CCP profile, see Zhao et al., 2015 supplementary material). Furthermore, the stations that should best detect this small amplitude signal from a deep European Moho of the subducting European crust are located below the IGB and partially in the Po Plain, which, seismically speaking, are very noisy areas. Seismological evidence in support of a continuous subducting LAB below the Western Alps is proposed by Malusà et al. (2021), who interpreted the profile by Lyu et al. (2017). In this interpretation the LAB interface is extrapolated from the surface wave data, although, since there is no clear velocity jump, an objective LAB interface is hard to establish and it could be chosen in other ways that are not suggestive of subduction. In fact, the authors of the original paper, Lyu et al. (2017), mention the hypothesis of a deepening LAB, below 100 km depth, parallel to the Moho interface. They chose not pursue the hypothesis since they considered the area not well constrained by the data.

Even taking into account the resolution limited by the finite frequency of the waves, it is difficult to reconcile our observations with the present-day continuous subduction of the European lithosphere below the western Alps hypothesized by some authors. Furthermore, when we consider the geometries (gently dipping, quasi-horizontal LAB interface) and lengths that are involved, such as the lithospheric thicknesses (in the range of about 80–100 km in correspondence of the suture between the European and Adriatic plates) and the maximum distance between adjacent piercing points belonging to the two plates (that we can estimate in less than 40 km from our profiles in Figure 4), it is clear that there is hardly room for a continuous slab below this sector. If it exists, such a continuous slab should be dipping very steeply and be extremely thin in order to be completely overlooked by our analysis. The Moho measurements, which have a smaller Fresnel zone (about 35 km), reinforce this interpretation. Summarizing, all cross-sections in Figure 4 are consistent with collision of the European and Adria plates below the IGB area. In Figure 6 we show our results together with the outlines of the high velocity seismic anomalies of previously published tomography models. We find that our measurements match well the models of Kästle et al. (2018), a Vs velocity model for the crust and uppermost mantle derived from inversion of ambient noise and teleseismic surface waves, and Lippitsch et al. (2003), a Vp velocity model obtained from the inversion of teleseismic travel-times with accurate crustal corrections. Indeed, the trend of the LAB discontinuity detected from RF is consistent with the depth distribution of the Vp and Vs high velocity anomalies in these two models suggesting a slab detachment at shallow depths. Conversely, our robust detection of a quasi-horizontal LAB, cross-cutting at about 90 km depth the elongated high velocity anomaly imaged by Zhao et al. (2016), seems at odds with and would exclude the presence of a steeply dipping, continuous slab.

An interesting observation, although it comes from only a few available measurements, is that the LAB below the IGB appears to deepen, from about 80 km depth in the north, to about 100 km depth in the southern part (Figures 4a–4c). Such a difference in the discontinuity depth suggests that below the northern part of the IGB we are observing the Adria LAB, while in the southern part we are observing the European LAB. The IGB is considered as a piece of mantle wedge exhumed at lower crustal levels along the inner arc of the Western Alps, and partially outcropping at the surface in its north-eastern portion, known as the Ivrea Verbano Zone (e.g., Schmid et al., 2017). Our finding about a shallower LAB depth observed at the stations located in the northeast is therefore intriguing and is another element in favor of a tight connection between the deep structure of the lithosphere-asthenosphere system and the near-surface tectonic features in this region already mentioned by other authors (e.g., Kissling et al., 2006). However, given the scarcity of available data for the IGB, we prefer to not further interpret this observation and wait for future detailed analyses and new experiments with sufficiently dense recordings of teleseismic data. To appreciate how receiver functions can investigate the finer structure of the IGB, it is important to more accurately determine their lateral resolution by using a more complex theoretical treatment than the Fresnel zone, such as scattering theory, which is not trivial. It has been shown that different quantities that describe the observation of converted waves have different sensitivity spatial patterns. For example, the sensitivity kernel of the traveltime of a body wave propagating in a spherically symmetric Earth has the shape of a banana-donut (e.g., Marquering et al., 1999) and is zero along the raypath, while, on the other hand, the amplitude kernel has maximum sensitivity along the raypath (Dahlen & Baig, 2002). Hansen and Schmandt (2017) demonstrated the potential of the kernel imaging approach applied to both P and S receiver

Figure 4. Moho and Lithosphere-Asthenosphere Boundary (LAB) depth cross-sections for the traces shown in Figure 1. Circles indicate the S-to-p piercing points and squares the P-to-s piercing points-red Moho and green LAB. The piercing points are calculated from the station stacks (PRF and SRF) for average distances. Vertical bars are the errors calculated from the Gaussian fit. Horizontal bars represent the extension of the first Fresnel zone. The blue curves are an interpolation of the Moho values published by Spada et al. (2013). For each cross section the moho and LAB depth values of stations within ±90 km from the projection plane are shown. AF, Alpine front; WA, Western Alps; IGB, Ivrea Geophysical Body; AD, Adria.

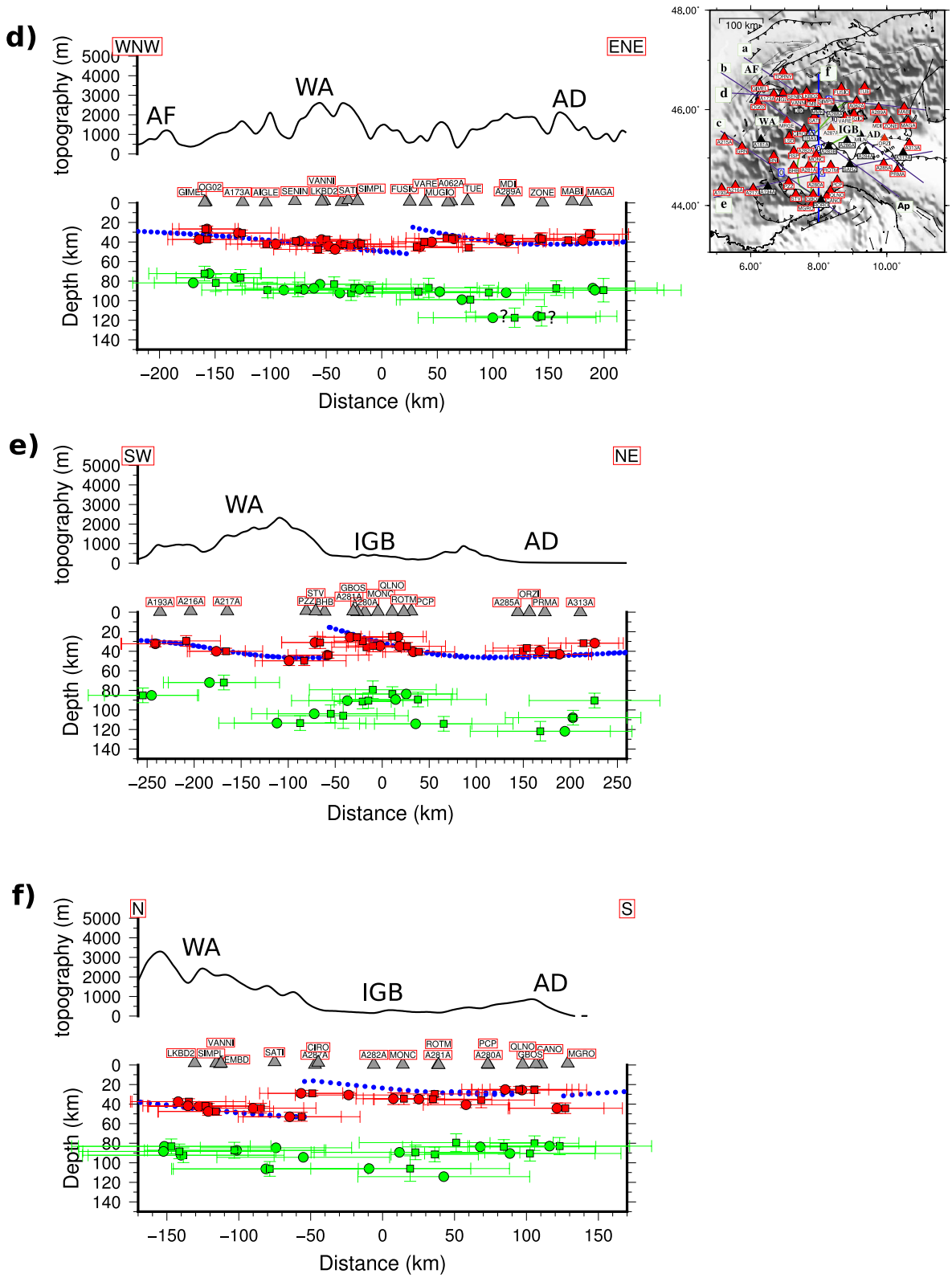

Figure 4. (Continued)

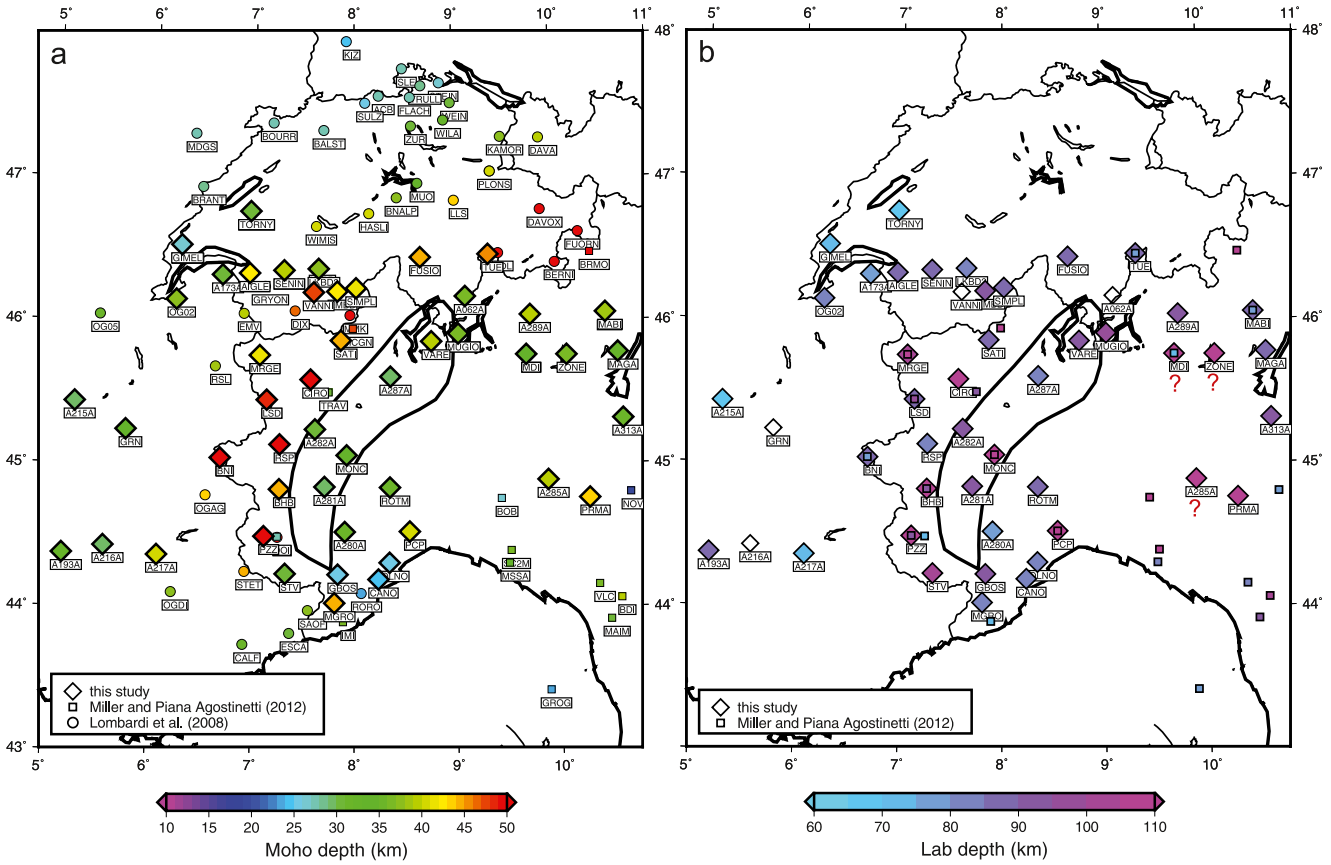

Figure 5. Maps with (a) Moho depth calculated in our study (diamonds) compared with the measurements of Miller and Piana Agostinetti (2012) (squares) and Lombardi et al. (2008) (circles) and (b) our values of the Lithosphere-Asthenosphere Boundary depth (diamonds) compared with the measurements (squares) by Miller and Piana Agostinetti (2012).

functions to constrain lithospheric structure in complex geologic environments and image compositional variations in the mantle wedge and the slab's lithosphere-asthenosphere boundary.

5. Conclusions

We applied a non-linear joint inversion of P and S receiver functions to calculate seismic velocity models below a set of stations of the AlpArray Seismic Network, located in the Western Alps. From the models of 50 stations we were able to estimate the Moho and LAB depths. Great attention was paid to data selection and processing to obtain reliable signals converted from the Moho and LAB. The inversion procedure was based on a careful analysis of the model space, in particular we applied general sensitivity analysis to optimize the dimension of the parameter space. This study, while confirming the Moho trend from previous works, adds new, dense measurements of the LAB depth that were previously not available for this area. In addition, the 1D velocity models we obtained from the joint inversion of data from the 50 stations could be used in future studies to construct a priori 3D velocity models for the Western Alps area.

We find a gradual deepening of the European LAB (and Moho) going from west to east, up to the Ivrea Geophysical Body (IGB). Consistently with previous works, we observe that the European Moho at the IGB is deeper than the Adria Moho. We also find that across the IGB the depths of the newly determined LAB of the two plates are remarkably similar, at about 90–100 km. In the Adria plate LAB and Moho attain their deepest value below the Apennines. Our observations are difficult to reconcile with the present-day continuous subduction of the European lithosphere below the Western Alps postulated by some studies, and they are more consistent with a collision of the European and Adria plates below the Ivrea Geophysical Body and a slab detachment at shallow depth.

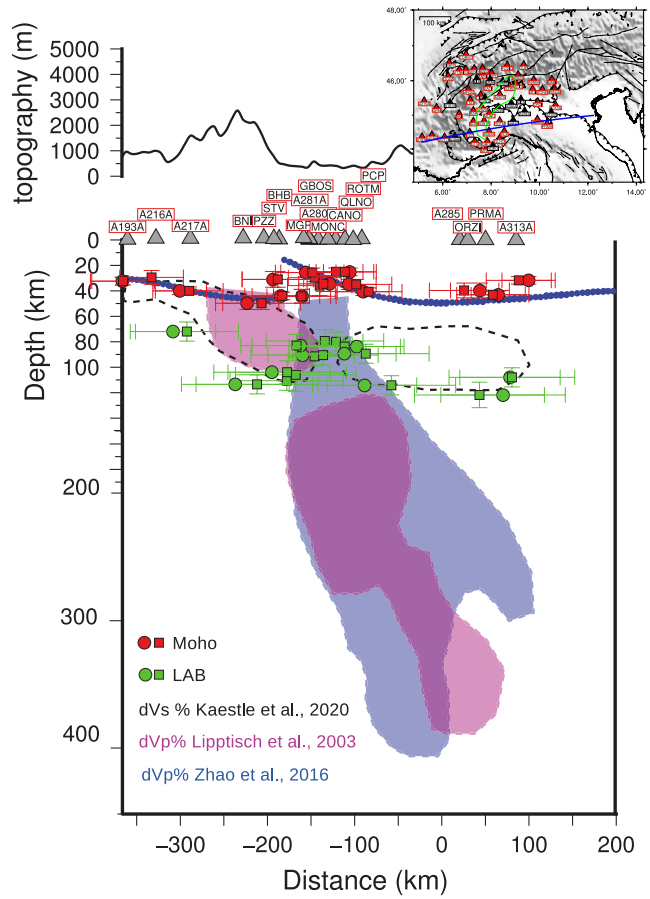

Figure 6. Moho (red symbols) and Lithosphere-Asthenosphere Boundary (LAB) (green symbols) depth for a profile (shown in the inset) very close to cross-section A (Western Alps) of Figure 3 in Kästle et al. (2020). The outlined high seismic velocity anomalies are retraced from three of the models shown in the same figure: in magenta Vp% from Lippitsch et al. (2003), in blue Vp% from Zhao et al. (2016), in black Vs% from Kästle et al. (2018). Blue circles is the Moho depth from Spada et al. (2013). The trend of the LAB discontinuity detected from RF in this study cross-cuts at about 90 km depth the elongated high velocity anomaly imaged by Zhao et al. (2016), while is consistent with the depth distribution of the Vp and Vs high velocity anomalies in the two models imaging a slab detachment at shallow depths. The quasi-horizontal and continuous LAB trend seems at odds with the presence of a steeply dipping slab continuous up to the surface.

Appendix A

A.1. Joint Inversion of P and S Receiver Functions

The calculation of the velocity models, which includes a forward part and an inversion part, is based on the following steps:

1. We consider an input model composed of five plane layers of variable thickness defined by Vp and Vs values that joins the IASP91 model (Kennett & Engdahl, 1991) below. For each randomly generated model synthetic P and S receiver functions are calculated using the same steps applied for the real data receiver functions. More detailed information on the forward part of the process, which uses the software package "Computer Programs in Seismology" (Herrmann, 2013) for synthetic seismograms calculation, and the software "Seismic Handler" (Stammler, 1993) for the calculation of the receiver functions and their stacks, are given in Monna et al. (2019).
2. The joint inversion of P and S receiver functions is performed by the Generalized Simulated Annealing method, which is based on the Tsallis statistics (Tsallis, 1988; Tsallis & Stariolo, 1996). We apply the *dual_anneal* function part of the SciPy "optimize" sub-package (Virtanen et al., 2020) based on the GenSA implementation of the Generalized Simulated Annealing derived from Xiang et al. (1997, 2013). We define the energy

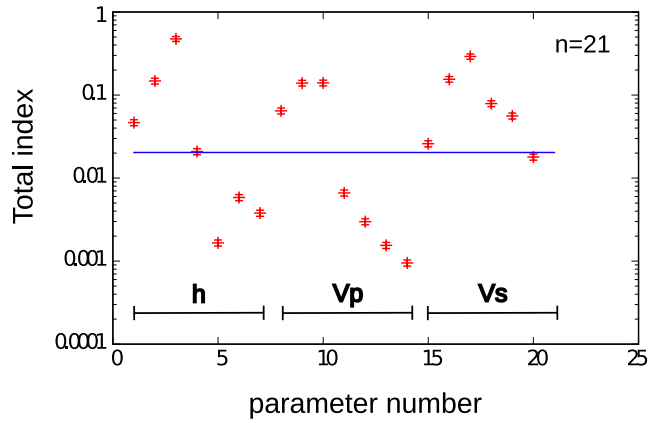

Figure A1. Total indices in the case $n = 21$ (7 Earth layers) calculated for station QLNO. h (parameters 1–7) is the layer thickness. Vp (parameters 8–14) and Vs (parameters 15–21) are the P and S velocity in each corresponding layer.

function to be minimized as the cross-correlation (Pearson), between the synthetic and observed receiver functions. The P and S RF are weighted in the same way in the energy function. Up to $\sim 10^5$ models from the parameter space might be sampled to find the global minimum of the energy function.

A.2. Generalized Sensitivity Analysis

To perform General Sensitivity Analysis on our inversion problem we applied codes that are based on the variance formulation of Sobol (1993, 2001). In this formulation the variance of the output variable Y (which in our case represents the energy function) is decomposed in the following way (Saltelli et al., 2008):

$$V(Y) = \sum_i V_i + \sum_i \sum_{i>j} V_{ij} + \ldots + V_{1\ldots n} \tag{A1}$$

Where $V_i = V(E(X_i))$ measures the effect of variable X_i on Y by itself (E is the expected value). The term

$$V_{ij} = V(E(X_i, X_j)) - V(E(X_i)) - V(E(X_j)) = V(E(X_i, X_j)) - V_i - V_j$$

measures the joint effect of the pair (X_i, X_j) on Y (Saltelli et al., 2004), and similarly for the higher order interactions, for example,

$$V_{ijk} = V(E(X_i, X_j, X_k)) - V_{ij} - V_{ik} - V_{jk} - V_i - V_j - V_k$$

measures the joint effect of the triplet(X_i, X_j, X_k)on Y and so on for the higher order terms.

Dividing both sides of Equation A1 by V(Y) and introducing the sensitivity indices we have:

$$\sum_i S_i + \sum_i \sum_{i>j} S_{ij} + \ldots + S_{1\ldots n} = 1 \tag{A2}$$

The first-order (or primary) sensitivity index S_i describes the effect that variable X_i has on the output variance by itself, excluding the interactions it might have with the other variables. In a model without interactions only the terms $V_i, V_j \ldots V_n$ are different from 0. The calculation of all the sensitivity indices in Equation A2 can be computationally prohibitive for problems with a large number of parameters.

A direct consequence of Sobol's variance decomposition is the introduction of the total effect index which takes into account the total effect of an input variable on the output by itself and through all possible interactions with the other input variables (Saltelli et al., 2008 and references therein). As, an example, in the case of 3 variables the total effect for input variable X_1 is (Equation 4.13 in Saltelli et al., 2008) $S_{T1} = S_1 + S_{12} + S_{13} + S_{123}$

The difference S_{Ti}-S_i is a useful quantity that measures how much variable X_i interacts with the other variables. The condition $S_{Ti} = 0$ is necessary and sufficient to establish that variable X_i has no influence on the output and if $S_{Ti} \cong 0$, then we can fix $X_i$within its interval of uncertainty (Saltelli et al., 2008). Furthermore, the total indices

can be calculated through efficient Montecarlo methods at the same computational cost of the primary indices S_i (see Saltelli et al., 2008 and references therein).

To calculate the primary and total indices we have applied the GSA *sobolmartinez* function included in the "sensitivity" R package (Iooss et al., 2020) and written some code to implement the GSA algorithm to our case. The *sobolmartinez* function uses a Monte Carlo Estimation of Sobol indices based on the formulas of Martinez (2011). As a practical example we consider a parameter space that represents an Earth with 7 layers with varying thickness and Vp and Vs values, so in total we have $n = 7*3 = 21$ parameters to invert. After performing GSA analysis for several stations we could see that several parameters are either uninfluential ($S_{Ti} = 0$) or barely influential ($S_{Ti} \cong 0$), and that we can safely bring down the number of layers to 5, reducing the overall number of parameters to $n = 5*3 = 15$. The overall number of parameters could possibly be reduced even further, depending on the dataset, but we verified that for the stations used in this study 15 is an appropriate choice. Figure A1 shows the total indices in the case $n = 21$ (7 Earth layers) calculated for station QLNO. One can see that many parameters have total indices near zero (index 21 is outside the figure range since it is = 0). If we choose 0.02 as threshold for which we can consider the indices below this value as uninfluential, then there are 12 parameters that are above the threshold and are able to adequately describe the variance of the energy function. As a safe choice we decided to invert for 5 layers, which means $n = 5*3 = 15$ parameters.

For a rigorous treatment of Sobol's theory and a general treatment of GSA we refer the interested reader to Sobol's original papers (1993, 2001) and to Saltelli et al. (2004, 2008).

A.3. Authors of AlpArray Working Group

Members of the AlpArray Seismic Network Team: György Hetényi, Rafael Abreu, Ivo Allegretti, Maria-Theresia Apoloner, Coralie Aubert, Simon Besançon, Maxime Bès De Berc, Götz Bokelmann, Didier Brunel, Marco Capello, Martina Čarman, Adriano Cavaliere, Jérôme Chèze, Claudio Chiarabba, John Clinton, Glenn Cougoulat, Wayne C. Crawford, Luigia Cristiano, Tibor Czifra, Ezio D'alema, Stefania Danesi, Romuald Daniel, Anke Dannowski, Iva Dasović, Anne Deschamps, Jean-Xavier Dessa, Cécile Doubre, Sven Egdorf, Ethz-Sed Electronics Lab, Tomislav Fiket, Kasper Fischer, Wolfgang Friederich, Florian Fuchs, Sigward Funke, Domenico Giardini, Aladino Govoni, Zoltán Gráczer, Gidera Gröschl, Stefan Heimers, Ben Heit, Davorka Herak, Marijan Herak, Johann Huber, Dejan Jarić, Petr Jedlička, Yan Jia, Hélène Jund, Edi Kissling, Stefan Klingen, Bernhard Klotz, Petr Kolínský, Heidrun Kopp, Michael Korn, Josef Kotek, Lothar Kühne, Krešo Kuk, Dietrich Lange, Jürgen Loos, Sara Lovati, Deny Malengros, Lucia Margheriti, Christophe Maron, Xavier Martin, Marco Massa, Francesco Mazzarini, Thomas Meier, Laurent Métral, Irene Molinari, Milena Moretti, Anna Nardi, Jurij Pahor, Anne Paul, Catherine Péquegnat, Daniel Petersen, Damiano Pesaresi, Davide Piccinini, Claudia Piromallo, Thomas Plenefisch, Jaroslava Plomerová, Silvia Pondrelli, Snježan Prevolnik, Roman Racine, Marc Régnier, Miriam Reiss, Joachim Ritter, Georg Rümpker, Simone Salimbeni, Marco Santulin, Werner Scherer, Sven Schippkus, Detlef Schulte-Kortnack, Vesna Šipka, Stefano Solarino, Daniele Spallarossa, Kathrin Spieker, Josip Stipčević, Angelo Strollo, Bálint Süle, Gyöngyvér Szanyi, Eszter Szűcs, Christine Thomas, Martin Thorwart, Frederik Tilmann, Stefan Ueding, Massimiliano Vallocchia, Luděk Vecsey, René Voigt, Joachim Wassermann, Zoltán Wéber, Christian Weidle, Viktor Wesztergom, Gauthier Weyland, Stefan Wiemer, Felix Wolf, David Wolyniec, Thomas Zieke, Mladen Živčić and Helena Žlebčíková.

More information on AlpArray can be found at www.alparray.ethz.ch.

Data Availability Statement

Data come from a subset of temporary and permanent stations of the broadband AlpArray Seismic Network (2015) https://doi.org/10.1007/s10712-018-9472-4. Data from the temporary stations (network Z3) can be accessed through http://data.datacite.org/10.12686/alparray/z3_2015. Data from the permanent stations come from the following seismic networks: CH-Swiss Seismological Service (SED) at ETH Zurich; (1983): National Seismic Networks of Switzerland; ETH Zürich. https://doi.org/10.12686/sed/networks/ch; IV-INGV Seismological Data Centre. (1997). Rete Sismica Nazionale (RSN). Istituto Nazionale di Geofisica e Vulcanologia (INGV), Italy. http://doi.org/10.13127/SD/X0FXnH7QfY; FR-RESIF. (1995). RESIF-RLBP French Broad-band network, RESIF-RAP strong motion network and other seismic stations in metropolitan France. RESIF-Réseau

Acknowledgments
We acknowledge the operation of the AlpArray temporary seismic network Z3, see Hetényi et al. (2018) and AlpArray Seismic Network (2015) and the permanent seismic networks used in this study: AC (Albanian seismic network, Institute of Geosciences, Polytechnic University of Tirana), BA (Universita della Basilicata Seismic Network), BE (Royal Observatory of Belgium 1985), BS (National Institute of Geophysics, Geodesy and Geography - BAS 1980), BW (Department of Earth and Environmental Sciences, Geophysical Observatory, University of Munchen 2001), CA (Institut Cartogràfic i Geològic de Catalunya-Institut d'Estudis Catalans 1996), CR (Croatian seismograph network, University of Zagreb), CZ (Institute of Geophysics, Academy of Sciences of the Czech Republic 1973), ES (Spanish digital seismic network, Subdireccion General De Geodesia Y Geofisica), FR - RESIF (Réseau Sismologique et géodésique Français 1995), G (Institut de physique du Globe de Paris and Ecole et observatoire des sciences de la terre de Strasbourg 1982), GB (Great Britain seismograph network, British Geological Survey), GE (GEOFON Data Centre 1993), GR (German Regional Seismic Network, Federal Institute for Geosciences and Natural Resources), GU (University of Genova 1967), HL (National Observatory of Athens, Institute of Geodynamics 1997), HU (Kövesligethy Radó Seismological Observatory, Geodetic And Geophysical Institute, Research Centre For Astronomy And Earth Sciences, Hungarian Academy Of Sciences 1992), CH (Swiss Seismological Service, ETH Zurich 1983), IV (Istituto Nazionale di Geofisica e Vulcanologia 2006), IX (Irpinia Seismic Network, Unit of experimental and computational seismology, Physics Department, University of Naples Federico II, Italy), LC (Laboratorio Subterraneo de Canfranc, Spain 2011), ME (Institute of Hydrometeorology and Seismology of Montenegro 1982), MN (MedNet Project Partner Institutions 1990), MT (National French Landslide Observatory Facility and Reseau sismologique et géodésique français datacenter 2006), NI (Istituto Nazionale di Oceanografia e di Geofisica Sperimentale and University of Trieste 2002), NL (Royal Netherlands Meteorological Institute 1993), OE (Seismic network of Austria, Zentralanstalt für Meteorologie und Geodynamik, Austria 1987), OT (University of Bari "Aldo Moro" 2013), OX (Istituto Nazionale di Oceanografia e di Geofisica Sperimentale 2016), PL (Polish seismological network, Institute of Geophysics, Polish Academy of Sciences), RD (Réseau Sismologique et géodésique Français 2018), RO (National Institute for Earth Physics, Romania 1994), SI (Province Südtirol, Zentralanstalt für Meteorologie und Geodynamik, sismologique & géodésique français. http://doi.org/10.15778/RESIF.FR; GU-University of Genova (1967): Regional Seismic Network of North Western Italy. International Federation of Digital Seismograph Networks. Other/Seismic Network. http://doi.org/10.7914/SN/GU. Three years after operation of the AlpArray Seismic Network has ended (starting 1 April 2022) the waveform data will be freely available to the public (http://www.alparray.ethz.ch/en/seismic_network/backbone/data-policy-and-citation/). We downloaded station data from http://www.orfeus-eu.org/data/eida/. Figures were generated with the open source software gnuplot (http://www.gnuplot.info); Inkscape (http://www.inkscape.org/); GMT (Wessel & Smith, 1991; https://www.generic-mapping-tools.org/). Calculation of synthetic seismograms was performed using the software package "Computer Programs in Seismology" (Herrmann, 2013; available for download at https://www.eas.slu.edu/eqc/eqccps.html). Calculation of receiver function and stacks (both observed and synthetic) were performed with the software Seismic Handler (Stammler, 1993; available for download at https://www.seismic-handler.org/). Joint inversion of receiver functions was performed with the *dual_anneal* function part of the SciPy "optimize" sub-package (Virtanen et al., 2020; available for download at https://docs.scipy.org/doc/scipy/tutorial/optimize.html). General sensitivity analysis was performed with the function *sobolmartinez* part of the "sensitivity" R package (Iooss et al., 2020; available for download at https://www.rdocumentation.org/packages/sensitivity/versions/1.27.0).

References

AlpArray Working Group. AlpArray seismic network (AASN) temporary component. https://doi.org/10.12686/ALPARRAY/Z3_2015

Ammon, C. J., Randall, G. E., & Zandt, G. (1990). On the nonuniqueness of receiver function inversions. *Journal of Geophysical Research*, *95*(B10), 15303–15318. https://doi.org/10.1029/JB095iB10p15303

Beller, S., Monteiller, V., Operto, S., Nolet, G., Paul, A., & Zhao, L. (2017). Lithospheric architecture of the South-Western Alps revealed by multiparameter teleseismic full-waveform inversion. *Geophysical Journal International*, *212*(2), 1369–1388. https://doi.org/10.1093/gji/ggx216

Blanckenburg, F., & Davies, J. H. (1995). Slab breakoff: A model for syncollisional magmatism and tectonics in the Alps. *Tectonics*, *14*(1), 120–131. https://doi.org/10.1029/94tc02051

Bodin, T., Sambridge, M., Tkalčić, H., Arroucau, P., Gallagher, K., & Rawlinson, N. (2012). Transdimensional inversion of receiver functions and surface wave dispersion. *Journal of Geophysical Research*, *117*(B02301). https://doi.org/10.1029/2011JB008560

Cerveny, V. (2001). *Seismic ray theory*. Cambridge University Press. https://doi.org/10.1017/CBO9780511529399

Crotwell, H. P., Owens, T. J., & Ritsema, J. (1999). The TauP toolkit: Flexible seismic travel-time and ray-path utilities. *Seismological Research Letters*, *70*(2), 154–160. https://doi.org/10.1785/gssrl.70.2.154

Dahlen, F. A., & Baig, A. M. (2002). Fréchet kernels for body-wave amplitudes. *Geophysical Journal International*, *150*(2), 440–466. https://doi.org/10.1046/j.1365-246X.2002.01718.x

Davies, J. H., & von Blanckenburg, F. (1995). Slab breakoff: A model of lithosphere detachment and its test in the magmatism and deformation of collisional orogens. *Earth and Planetary Science Letters*, *129*(1–4), 85–102. https://doi.org/10.1016/0012-821x(94)00237-s

Dercourt, J., Zonenshain, L. P., Ricou, L.-E., Kazmin, V. G., Le Pichon, X., Knipper, A. L., et al. (1986). Geological evolution of the Tethys Belt from the Atlantic to the Pamirs since the Lias. *Tectonophysics*, *123*(1–4), 241–315. https://doi.org/10.1016/0040-1951(86)90199-X

Di Stefano, R., Bianchi, I., Ciaccio, M. G., Carrara, G., & Kissling, E. (2011). Three-dimensional Moho topography in Italy: New constraints from receiver functions and controlled source seismology. *Geochemistry, Geophysics, Geosystems*, *12*(9), Q09006. https://doi.org/10.1029/2011GC003649

Farra, V., & Vinnik, L. (2000). Upper mantle stratification by P and S receiver functions. *Geophysical Journal International*, *141*(3), 699–712. https://doi.org/10.1046/j.1365-246x.2000.00118.x

Fox, M., Herman, F., Kissling, E., & Willett, S. D. (2015). Rapid exhumation in the Western Alps driven by slab detachment and glacial erosion. *Geology*, *43*(5), 379–382. https://doi.org/10.1130/g36411.1

Geissler, W. H., Sodoudi, F., & Kind, R. (2010). Thickness of the central and eastern European lithosphere as seen by S receiver functions. *Geophysical Journal International*, *181*, 2604–2634. https://doi.org/10.1111/j.1365-246X.2010.04548.x

Hansen, S. M., & Schmandt, B. (2017). P and S wave receiver function imaging of subduction with scattering kernels. *Geochemistry, Geophysics, Geosystems*, *18*(12), 4487–4502. https://doi.org/10.1002/2017GC007120

Herrmann, R. B. (2013). Computer programs in seismology: An evolving tool for instruction and research. *Seismological Research Letters*, *84*(6), 1081–1088. https://doi.org/10.1785/0220110096

Hetényi, G., Molinari, I., Clinton, J., Bokelmann, G., Bondar, I., Crawford, W. C., et al. (2018). The AlpArray seismic network: A large-scale European experiment to image the Alpine orogeny. *Surveys in Geophysics*, *39*(5), 1009–1033. https://doi.org/10.1007/s10712-018-9472-4

Iooss, B., Veiga, S. D., Janon, A., Pujol, G., wcfB, B., Boumhaout, K., et al. (2020). Sensitivity: Global sensitivity analysis of model outputs. R package version 1.20.0. Retrieved from https://CRAN.R-project.org/package=sensitivity

Kästle, E. D., El-Sharkawy, A., Boschi, L., Meier, T., Rosenberg, C., Bellahsen, N., et al. (2018). Surface wave tomography of the Alps using ambient-noise and earthquake phase velocity measurements. *Journal of Geophysical Research*, *123*(2), 1770–1792. https://doi.org/10.1002/2017JB014698

Kästle, E. D., Rosenberg, C., Boschi, L., Bellahsen, N., Meier, T., & El-Sharkawy, A. (2020). Slab break-offs in the Alpine subduction zone. *International Journal of Earth Sciences*, *109*(2), 587–603. https://doi.org/10.1007/s00531-020-01821-z

Kennett, B. L. N., & Engdahl, E. R. (1991). Traveltimes for global earthquake location and phase identification. *Geophysical Journal International*, *105*(2), 429–465. https://doi.org/10.1111/j.1365-246X

Kind, R., Schmid, S., Yuan, X., Heit, B., Meier, T., & WorkingAlparray-Swath, -D. (2021). Moho and uppermost mantle structure in the Alpine area from S-to-P converted waves. *Solid Earth*, *12*(11), 2503–2521. https://doi.org/10.5194/se-12-2503-2021

Kind, R., & Vinnik, L. P. (1988). The upper mantle discontinuities underneath the GRF array from P-to-S converted phases. *Journal of Geophysics*, *62*, 138–147.

Austria), SJ (Serbian seismological network, Seismological survey of Serbia), SK (Earth Science Institute, Slovak academy of sciences 2004), SL (Slovenian Environment Agency 2001), ST (Geological Survey, Provincia Autonoma di Trento 1981), SX (Leipzig University 2001), TH (Thüringer Seismologisches Netz, Friedrich-Schiller-Universität Jena 2009), WM (Western Mediterranean Seismic Network, San Fernando Royal Naval Observatory (Spain), Universidad Complutense De Madrid (Spain), Helmholtz-Zentrum Potsdam Deutsches GeoForschungsZentrum (Germany), Universidade De Evora (Portugal) and Institute Scientifique of RABAT (Morocco) 1996). This work has been supported by the INGV grant Pianeta Dinamico (code CUP D53J19000170001) funded by the Italian Ministry of University and Research "Fondo finalizzato al rilancio degli investimenti delle amministrazioni centrali dello Stato e allo sviluppo del Paese, legge 145/2018". We thank two anonymous reviewers who helped improve an earlier version of the manuscript. Open Access Funding provided by Istituto Nazionale di Geofisica e Vulcanologia within the CRUI-CARE Agreement.

Kiselev, S., Vinnik, L., Oreshin, S., Gupta, S., Rai, S. S., Singh, A., et al. (2008). Lithosphere of the Dharwar craton by joint inversion of P and S receiver functions. *Geophysical Journal International*, *173*(3), 1106–1118. https://doi.org/10.1111/j.1365-246X.2008.03777.x

Kissling, E., Schmid, S. M., Lippitsch, R., Ansorge, J., & Fügenschuh, B. (2006). Lithosphere structure and tectonic evolution of the Alpine arc: New evidence from high-resolution teleseismic tomography. *Geological Society, London, Memoirs Home*, *32*(1), 129–145. https://doi.org/10.1144/gsl.mem.2006.032.01.08

Liao, J., Gerya, T., & Malusà, M. G. (2018). 3D modeling of crustal shortening influenced by along-strike lithological changes: Implications for continental collision in the western and Central Alps. *Tectonophysics*, *746*, 425–438. https://doi.org/10.1016/j.tecto.2018.01.031

Lippitsch, R., Kissling, E., & Ansorge, J. (2003). Upper mantle structure beneath the Alpine orogen from high-resolution teleseismic tomography. *Journal of Geophysical Research*, *108*(B8), 2376. https://doi.org/10.1029/2002JB002016

Lombardi, D., Braunmiller, J., Kissling, E., & Giardini, D. (2008). Moho depth and Poisson's ratio in the Western-Central Alps from receiver functions. *Geophysical Journal International*, *173*(1), 249–264. https://doi.org/10.1111/j.1365-246x.2007.03706.x

Lyu, C., Pedersen, H. A., Paul, A., Zhao, L., & Solarino, S. (2017). Shear wave velocities in the upper mantle of the Western Alps: New constraints using array analysis of seismic surface waves. *Geophysical Journal International*, *210*(1), 321–331. https://doi.org/10.1093/gji/ggx166

Malusà, M. G., Guillot, S., Zhao, L., Paul, A., Solarino, S., Dumont, T., et al. (2021). The deep structure of the Alps based on the CIFALPS seismic experiment: A synthesis. *Geochemistry, Geophysics, Geosystems*, *22*(3), e2020GC009466. https://doi.org/10.1029/2020GC009466

Marquering, H., Dahlen, F., & Nolet, G. (1999). Three-dimensional sensitivity kernels for finite-frequency traveltimes: The banana–doughnut paradox. *Geophysical Journal International*, *137*(3), 805–815. https://doi.org/10.1046/j.1365-246x.1999.00837.x

Martinez, M. (2011). Analyse de sensibilite globale par decomposition de la variance. In *Presentation in the meeting of GdR Ondes and GdR MASCOT-NUM, 13th, January, 2011*. Institut Henri Poincare.

Miller, M. S., & Piana Agostinetti, N. (2012). Insights into the evolution of the Italian lithospheric structure from S receiver functions. *Earth and Planetary Science Letters*, *345*, 49–59. https://doi.org/10.1016/j.epsl.2012.06.028

Monna, S., Montuori, C., Piromallo, C., & Vinnik, L. (2019). Mantle structure in the central Mediterranean region from P and S receiver functions. *Geochemistry, Geophysics, Geosystems*, *20*(10), 4545–4566. https://doi.org/10.1029/2019GC008496

Morais, I., Vinnik, L., Silveira, G., Kiselev, S., & Matias, L. (2015). Mantle beneath the Gibraltar Arc from receiver functions. *Geophysical Journal International*, *200*(2), 1155–1171. https://doi.org/10.1093/gji/ggu456

Nocquet, J. M., Sue, C., Walpersdorf, A., Tran, T., Lenôtre, N., Vernant, P., et al. (2016). Present-day uplift of the Western Alps. *Scientific Reports*, *6*(1), 28404. https://doi.org/10.1038/srep28404

Paffrath, M., Friederich, W., Schmid, S. M., & Handy, M. R. (2021). Imaging structure and geometry of slabs in the greater Alpine area—A P-wave traveltime tomography using AlpArray Seismic Network data. *Solid Earth*, *12*(11), 2671–2702. https://doi.org/10.5194/se-12-2671-2021

Saltelli, A., Ratto, M., Andres, T., Campolongo, F., Cariboni, J., Gatelli, D., et al. (2008). *Global sensitivity analysis: The primer*. John Wiley & Sons, Ltd.

Saltelli, A., Tarantola, S., Campolongo, F., & Ratto, M. (2004). *Sensitivity analysis in Practice: A guide to assessing scientific models*. John Wiley & Sons.

Schmid, S. M., Kissling, E., Diehl, T., van Hinsbergen, D. J. J., & Molli, G. (2017). Ivrea mantle wedge, arc of the Western Alps, and kinematic evolution of the Alps–Apennines orogenic system. *Swiss Journal of Geosciences*, *110*(2), 581–612. https://doi.org/10.1007/s00015-016-0237-0

Silveira, G., Vinnik, L., Stutzmann, E., Kiselev, S., Farra, V., & Morais, I. (2010). Stratification of the Earth beneath the Azores from P and S receiver functions. *Earth and Planetary Science Letters*, *229*(1–2), 91–103. https://doi.org/10.1016/j.epsl.2010.08.021

Sobol, I. M. (1993). Sensitivity analysis for non-linear mathematical models. *Mathematical Modelling in Civil Engineering*, *1*, 407–414. English translation of Russian original paper Sobol' (1990).

Sobol, I. M. (2001). Global sensitivity indices for nonlinear mathematical models and their Monte Carlo estimates. *Mathematics and Computers in Simulation*, *55*(1–3), 271–280. https://doi.org/10.1016/s0378-4754(00)00270-6

Spada, M., Bianchi, I., Kissling, E., Agostinetti, N. P., & Wiemer, S. (2013). Combining controlled-source seismology and receiver function infor-mation to derive 3-D Moho topography for Italy. *Geophysical Journal International*, *194*(2), 1050–1068. https://doi.org/10.1093/gji/ggt148

Spetzler, J., & Snieder, R. (2004). The Fresnel volume and transmitted waves. *Geophysics*, *69*(3), 653–663. https://doi.org/10.1190/1.1759451

Stammler, K. (1993). Seismic handler-programmable multichannel data handler for interactive and automatic processing of seismological analyses. *Computational Geosciences*, *2*, 135–140. https://doi.org/10.1016/0098-3004(93)90110-Q

Stampfli, G., Mosar, J., Favre, P., Pillevuit, A., & Vannay, J. C. (2001). Permo-Mesozoic evolution of the Western Tethys realm: The Neo-Tethys east Mediterranean basin connection. In *Peri-tethys Memoir* (Vol. 6, pp. 51–108). Peri-Tethyan Rift/Trench Basins And Passive Margins, Publ. Sci. du Mus.

Tsallis, C. (1988). Possible generalization of Boltzmann-Gibbs statistics. *Journal of Statistical Physics*, *52*(1–2), 479–487. https://doi.org/10.1007/bf01016429

Tsallis, C., & Stariolo, D. A. (1996). Generalized simulated Annealing. *Physica A: Statistical Mechanics and its Applications*, *233*(1), 395–406. https://doi.org/10.1016/s0378-4371(96)00271-3

Venables, W. N., & Ripley, B. D. (2002). *Modern applied statistics with S* (4th edn). Springer.

Vinnik, L. (1977). Detection of waves converted from P to SV in the mantle. *Physics of the Earth and Planetary Interiors*, *15*(1), 39–45. https://doi.org/10.1016/0031-9201(77)90008-5

Vinnik, L., & Farra, V. (2007). Low S velocity atop the 410 km discontinuity and mantle plumes. *Earth and Planetary Science Letters*, *262*(3), 398–412. https://doi.org/10.1016/j.epsl.2007.07.051

Vinnik, L., Silveira, G., Kiselev, S., Farra, V., Weber, M., & Stutzmann, E. (2012). Cape Verde hotspot from the upper crust to the top of the lower mantle. *Earth and Planetary Science Letters*, *319*, 259–268. https://doi.org/10.1016/j.epsl.2011.12.017

Vinnik, L. P., Farra, V., & Kind, R. (2004). Deep structure of the Afro-Arabian hotspot by S receiver functions. *Geophysical Research Letters*, *31*(11), L11608. https://doi.org/10.1029/2004GL019574

Virtanen, P., Gommers, R., Oliphant, T. E., Haberland, M., Reddy, T., Cournapeau, D., et al. (2020). SciPy 1.0: Fundamental Algorithms for scientific computing in Python. *Nature Methods*, *17*(3), 261–272. https://doi.org/10.1038/s41592-019-0686-2

Wagner, M., Kissling, E., & Husen, S. (2012). Combining controlled-source seismology and local earthquake tomography to derive a 3D crustal model of the Western Alpine region. *Geophysical Journal International*, *191*(2), 789–802. https://doi.org/10.1111/j.1365-246x.2012.05655.x

Waldhauser, F., Kissling, E., Ansorge, J., & Mueller, S. (1998). Three dimensional interface modelling with two-dimensional seismic data: The Alpine crust-mantle boundary. *Geophysical Journal International*, *135*(1), 264–278. https://doi.org/10.1046/j.1365-246X.1998.00647.x

Wessel, P., & Smith, W. H. (1991). Free software helps map and display data. *Eos Transactions American Geophysical Union*, *72*(41), 441. https://doi.org/10.1029/90eo00319

Xiang, Y., Gubian, S., Suomela, B., & Hoeng, J. (2013). Generalized simulated Annealing for efficient global optimization: The GenSA package for R. *The R Journal*, *5*(1), 13–29. https://doi.org/10.32614/rj-2013-002

Xiang, Y., Sun, D. Y., Fan, W., & Gong, X. G. (1997). Generalized simulated Annealing Algorithm and its Application to the Thomson model. *Physics Letters A*, *233*(3), 216–220. https://doi.org/10.1016/s0375-9601(97)00474-x

Zhao, L., Malusà, M. G., Yuan, H., Yuan, H., Paul, A., Guillot, S., et al. (2020). Evidence for a serpentinized plate interface favouring continental subduction. *Nature Communications*, *11*(1), 2171. https://doi.org/10.1038/s41467-020-15904-7

Zhao, L., Paul, A., Guillot, S., Solarino, S., Malusà, M. G., Zheng, T., et al. (2015). First seismic evidence for continental subduction beneath the Western Alps. *Geology*, *43*(9), 815–818. https://doi.org/10.1130/g36833.1

Zhao, L., Paul, A., & Solarino, S. (2016). CIFALPS temporary experiment (China-Italy-France Alps seismic transect). *RESIF-Réseau Sismologique et Géodésique Français*. https://doi.org/10.15778/RESIF.YP2012